The multiple *q*-vector incommensurate magnetic structure of $TbGe_3$

2007 J. Phys.: Condens. Matter 19 236201

(http://iopscience.iop.org/0953-8984/19/23/236201)

IOP PUBLISHING JOURNAL OF PHYSICS: CONDENSED MATTER

J. Phys.: Condens. Matter **19** (2007) 236201 (20pp) doi:10.1088/0953-8984/19/23/236201

The multiple q-vector incommensurate magnetic structure of $TbGe_3$

P Schobinger-Papamantellos[1], J Rodríguez-Carvajal[2] and K H J Buschow[3]

[1] Laboratory of Crystallography, ETH-Zurich, 8093 Zürich, Switzerland
[2] Institut Laue-Langevin, 156X, 38042 Grenoble Cédex, France
[3] Van der Waals-Zeeman Institute, University of Amsterdam, NL-1018 XE Amsterdam, Netherlands

E-mail: Schobinger@mat.ethz.ch and JRC@ill.fr

Received 8 February 2007, in final form 27 March 2007
Published 8 May 2007
Online at stacks.iop.org/JPhysCM/19/236201

Abstract

The magnetic phase diagram of the antiferromagnetic compound $TbGe_3$ (space group $Cmcm$, $T_N = 40$ K) has been studied by neutron diffraction and magnetic measurements. It comprises three distinct ranges of magnetic ordering characterized by two symmetry-independent wavevectors $\boldsymbol{q}_1 = (q_{1x}, 0, 0)$ and $\boldsymbol{q}_2 = (q_{2x}, 0, q_{2z})$ in addition to the paramagnetic state: the high-temperature (HT) range T_N down to $T_{ic} = 24$ K where $\boldsymbol{q}_1$ and $\boldsymbol{q}_2$ are incommensurate with the crystal lattice with variable length. In this range the magnetic structure corresponds to a planar $(0, y, z)$ modulated structure with variable amplitude and direction. Below $T_{ic} = 24$ K $\boldsymbol{q}_1$ and $\boldsymbol{q}_2$ lock in to the commensurate values $q_{1x} = q_{2x} = 1/2$ and $q_{2z} = 1/3$ corresponding to a sixfold cell enlargement $(2a, b, 3c)$ and a twofold splitting of the atomic positions. The magnetic space group (Shubnikov) is $P_bmma(Sh_{51}^{299})$. The two Tb sublattices are coupled antiferromagnetically. Their different temperature dependence is discussed in terms of a Fourier analysis of the observed data. The magnetic structure corresponds to a uniaxial antiphase domain moment arrangement $(+--)$ along c and $(+-)$ along a. In the intermediate-temperature (IT) range T_{ic} down to 16 K, μ_{Tb1}/μ_{Tb2} increases continuously from 0.87 to 1. In this range, the magnetic structure described by two amplitudes squares up to a constant-moment phase with 8.1 μ_B/Tb atom which persists in the low-temperature (LT) range 16–8 K.

(Some figures in this article are in colour only in the electronic version)

1. Introduction

In a previous investigation we reported on the crystal structure ($Cmcm$ space group $Z = 1$, with 3Ge and 1Tb sites at $4c$: $(0, y, 1/4)$) and on the magnetic ordering of the novel antiferromagnetic compound TbGe3, ($T_N = 40$ K) on the basis of powder neutron data [1].

Due to the allocated page restrictions the paper refers to only the temperature region 8 K $<$ T $<$ 23 K, where the magnetic structure is commensurate (C) with the crystal lattice and associated with a sixfold cell enlargement ($2a, b, 3c$) and a twofold splitting of the atomic positions [2]. Because all observed magnetic reflections (hkl) have $h = 2n + 1$ the C-centring operation is lost and the magnetic lattice becomes anti-centred along the a direction, P_a [3]. It is worth noting that the space group of the $3c$ enlarged cell $Cmcm$ is a maximal isomorphic subgroup of lowest index (order 3) of $Cmcm$.

In the enlarged cell the magnetic atoms occupy the sites Tb1 $8f$:$(0, y, z)$ with $z = 1/12$ in the ideal case and Tb2 $4c$: $(0, y, 1/4)$. The almost collinear magnetic moment arrangement is described by the non-standard setting magnetic space group P_amcm that was used in our calculations. It corresponds to the Shubnikov magnetic space group $P_bmma(Sh_{51}^{299})$ [3]. The atoms of the $4c$ site at the m_z mirror plane may have moments only along the c-direction while those of the $8f$ sites may have three components [1].

Alternatively, a superstructure can be described by Fourier expansion as a modulated magnetic structure of the basis cell P and for all observed branches of the wavevector(s) star participating in the transition. Symmetry analysis in terms of irreducible representations (Irreps) provides a useful tool in the reduction of the parameter space, provided no symmetry lowering has been observed. In our case the problem reduces to the description of the magnetic ordering of two Tb atoms at site $4c$ $m2m$:Tb_1: $(0, y, 1/4)$, Tb_2: $(0, -y, -1/4)$ and the wavevectors $\boldsymbol{q}_1 = (q_{1x}, 0, 0)$ and $\boldsymbol{q}_2 = (q_{2x}, 0, q_{2z})$. The atoms 3 and 4 of the conventional $Cmcm$ unit cell are obtained from (1) and (2) by adding the centring translation $\boldsymbol{t}_C = [1/2, 1/2, 0]$. This description is more general and is of importance in our case because the magnetic system in the HT range becomes incommensurate (IC) with the crystal lattice where the Shubnikov description does not apply.

The present paper serves a multiple purpose. (i) It increases the experimental information, by a new data set collected below and above T_N, with higher flux, high instrumental resolution (HR) and larger wavelength. We use this information to describe the model-independent behaviour of our system. We also present the magnetic measurements. (ii) We revise the previously published neutron diffraction results concerning the lock-in ordering (8–23 K) and extend our analysis to the HT range, from 24 K up to T_N. Our refinements are based on a magnetic structure model developed by symmetry analysis in terms of Irreps. (iii) We show the equivalence of the models obtained by the C and IC descriptions in detail at 8 K and comment on the various symmetry descriptions of such systems. Parts of point (ii) are given in the appendix while the phase problem in multiple $\boldsymbol{q}$-vector structures is discussed in its full generality by one of us (JRC) in a separate communication.

2. Experimental details

Magnetic measurements on $TbGe_3$ were made on a SQUID magnetometer in the temperature range 4.2–350 K. Results obtained are shown in figure 1. It is seen that Curie–Weiss behaviour of the reciprocal susceptibility (χ^{-1}) is observed down to about 100 K. From the slope of the reciprocal susceptibility curve above 100 K an effective moment of 10.4 μ_B/Tb atom was derived, which has to be compared to the value $g[J(J + 1)]^{1/2}\mu_B = 9.72\ \mu_B$ expected for trivalent Tb ions. The Curie–Weiss intercept equals $\theta p = -32$ K. The temperature dependence of the magnetization (σ) shows a cusp at $T_N = 40$ K, indicating antiferromagnetic ordering below this temperature.

Two sets of neutron diffraction data were collected and analysed by the *FullProf Suite* of programs [4]. The structure plots are made by the program *FullProf Studio* [5][4] incorporated

[4] *FullProf Studio* is a program of the *FullProf Suite* that is freely available in the site given in [4].

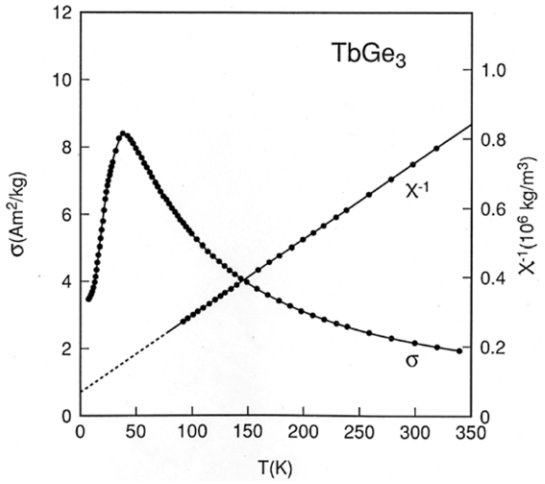

Figure 1. Temperature dependence of the magnetization σ (left scale) and temperature dependence of the reciprocal susceptibility (χ^{-1}, right scale) of $TbGe_3$. The data were obtained in a field of 1600 kA m^{-1}.

in [4]. One data set is an extension of the data of [1], collected with the DMC multicounter system at the reactor Saphir, Würenlingen ($\lambda = 1.7008$ Å, 2θ: 0–135° and step increment of 0.10°). This set regards the HT range and will be used in the refinements of the magnetic and crystal structures. The other data set was collected with the high-flux G6.1 multicounter system at the reactor Orphée (LLB, Saclay) with a larger wavelength ($\lambda = 4.741$ Å, 2θ: 10–90° and step increment of 0.20°) providing a high resolution at low Q in order to check for the presence of higher harmonics.

3. Results

3.1. High-resolution at low-Q neutron data ($\lambda = 4.741$ Å)

3.1.1. The magnetic satellites. Figure 2 displays some characteristic neutron patterns collected at various temperatures in the lock-in and the IC regions with $\lambda = 4.741$ Å. The few observed weak nuclear reflections, (0, 2, 0, 0, 4, 0, 1, 1, 0 and 0, 2, 1) display no changes of their intensities or 2θ positions. In contrast, the two sets of magnetic satellites $(h, k, l) \pm \boldsymbol{q}_i$ pertaining to the wavevectors $\boldsymbol{q}_1 = (q_{1x}, 0, 0)$ and $\boldsymbol{q}_2 = (q_{2x}, 0, q_{2z})$ display important changes of their intensities and 2θ peak positions above the lock-in temperature $T_{ic} = 24$ K. As reported in [1], below T_{ic} the wavevectors lock in to the values $q_{1x} = q_{2x} = 1/2$ and $q_{2z} = 1/3$. Furthermore, the neutron data comprise two unidentified reflections denoted by ($\mathbf{i}_1$ and $\mathbf{i}_2$) in figure 2 at $2\theta = 17.673°$ and 76.716° respectively. Both peaks appear below 43 K (see section 3.1.3) and display no significant position changes with temperature.

The $(0, k, 0) \pm \boldsymbol{q}_i$ satellites are seen to move towards smaller 2θ angles with increasing temperature above $T_{ic} = 24$ K, while the $\{1, 1, 0\}$-$\boldsymbol{q}_i$ satellites move to higher angles, indicating that the components of both wavevectors decrease with increasing temperature. This behaviour is more closely followed in figures 3(a) and (b). The position shift of both sets of satellites starts at about $T_{ic} = 24$ K, and marks the onset of the incommensurate region above this temperature.

Figure 3(c) shows that the q_{1x} and q_{2x} wavevector components derived from a complete data analysis using the profile matching tool of the program [4] have a very different temperature variation. The steepest decrease is just above the lock-in transition $T_{ic} = 24$ K.

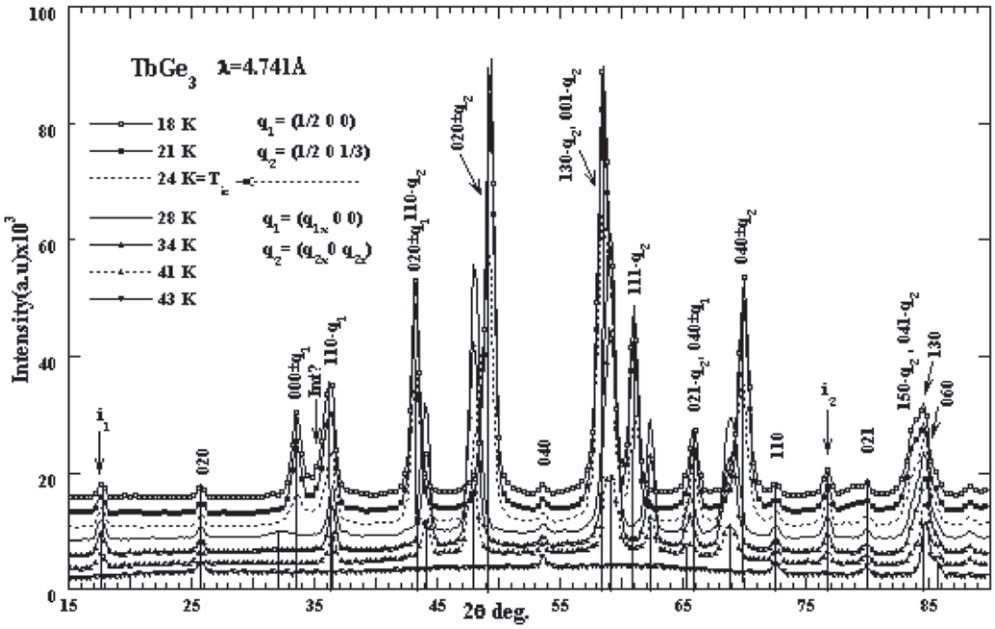

Figure 2. High-resolution neutron data (G6.1 instrument, $\lambda = 4.741$ Å) for various temperatures above and below the transition temperature to an incommensurate phase $T_{ic} = 24$ K.

The q_{1x} and q_{2z} components vary very slowly in the narrow range 24–26 K and level off very soon at 26.4 K within error to the commensurate values: $q_{1x} = 0.4928\ (7) \approx 31/63$ and $q_{2z} = 0.3258(6) \approx 13/40$. In contrast, the component q_{2x} experiences relatively larger changes with increasing temperature. At 29 K it has the value $q_{2x} = 0.4838(1) \approx 0.48 = 12/25$, and it slows down (slope change) at higher temperatures. The trajectory of the wavevector $\boldsymbol{q}_2$ in reciprocal space as a function of temperature does not deviate from a linear behaviour in the range 8–27 K (figure 3(d)).

3.1.2. Intensity versus T of the $\boldsymbol{q}_1$ *and* $\boldsymbol{q}_2$ *magnetic satellites.* The data displayed in figures 4(a) and (b) show that the $\boldsymbol{q}_1$ and $\boldsymbol{q}_2$ magnetic intensities exhibit quite different thermal variation. The strongest and only resolved $\boldsymbol{q}_1$ magnetic satellites ($(0, 0, 0)^{\pm}$ and $\{1, 1, 0\}^{-}$) are concentrated around $2\theta \approx 34°$. The integrated neutron intensity of the zero-point magnetic satellite $(0, 0, 0) \pm \boldsymbol{q}_1$, see figure 4(a), drops quickly to zero above T_{ic}, while the $(0, 0, 0) \pm \boldsymbol{q}_2$ satellite has zero intensity.

The intensity of the $(0, 0, 0) \pm \boldsymbol{q}_i$ satellites, in the particular case of $TbGe_3$, is independent of the atomic coordinates and gives first information about the relative phases and orientation of the magnetic moments (Fourier coefficients) of all atoms in the cell when we consider collinear structures. In our case we can, for instance, conclude from the behaviour of the $(0, 0, 0) \pm \boldsymbol{q}_1$ satellite that the Tb1 $(0y1/4)$ and Tb2 $(0-y3/4)$ magnetic moments have opposite signs with at least one component along b and/or c in the commensurate range. Then the structure factor for the reflection (1, 0, 0) in the $(2a, b, 3c)$ cell (table 2) is $4 f_{m\mathrm{Tb}^{3+}}(\boldsymbol{m}_1^{(\mathrm{Tb1})} + \boldsymbol{m}_2^{(\mathrm{Tb1})} + \boldsymbol{m}_3^{(\mathrm{Tb1})} + \boldsymbol{m}_4^{(\mathrm{Tb1})} + \boldsymbol{m}_1^{(\mathrm{Tb2})} + \boldsymbol{m}_2^{(\mathrm{Tb2})})$, which would be non-zero only for ferromagnetic modes and would decrease strongly only if $\boldsymbol{m}^{(\mathrm{Tb1})}$ and $\boldsymbol{m}^{(\mathrm{Tb2})}$ have opposite signs and $\boldsymbol{m}^{(\mathrm{Tb1})}$ becomes smaller than μ_{Tb2}. Similar arguments apply to the $(0, 0, 0) \pm \boldsymbol{q}_2$ satellite with zero intensity from the structure factor of the (1, 0, 1) reflection: in this case both sites have zero contribution for ferromagnetic modes.

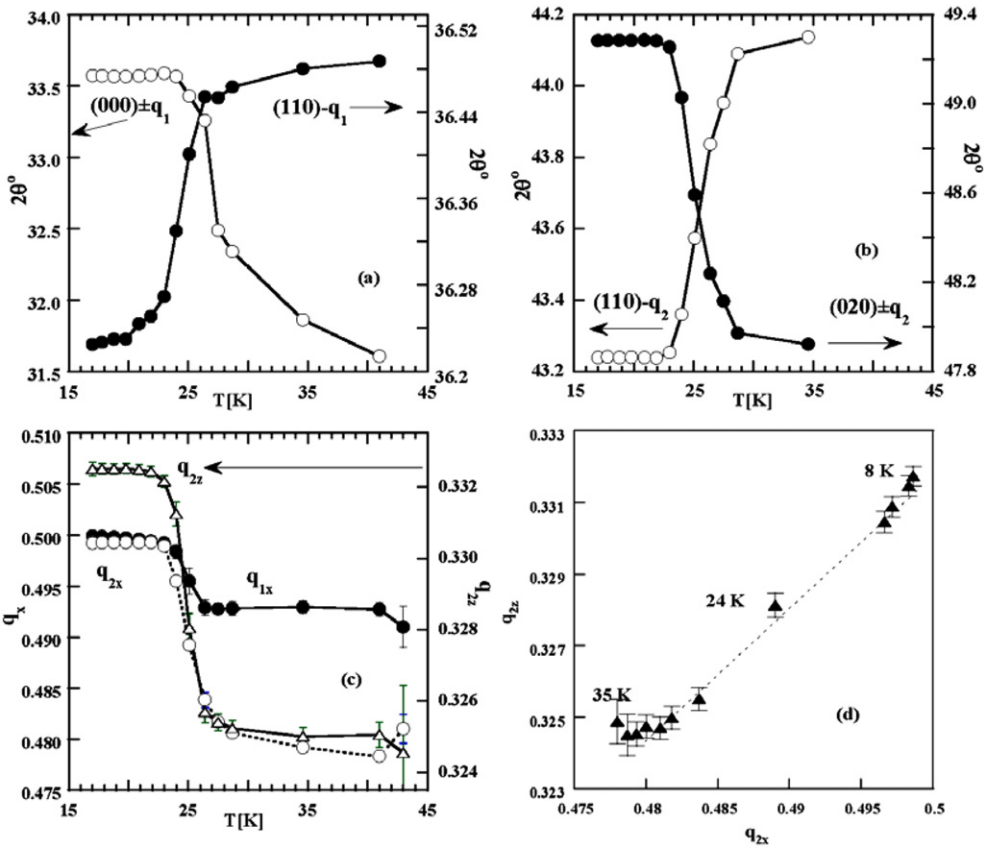

Figure 3. Thermal variation of the 2θ angles of several magnetic satellites associated with the wavevectors: (a) $\boldsymbol{q}_1 = (q_{1x}, 0, 0)$, (b) $\boldsymbol{q}_2 = (q_{2x}, 0, q_{2z})$ of $TbGe_3$. Also shown is the thermal variation of wavevector components: (c) and (d).

The $\{1, 1, 0\}$-$\boldsymbol{q}_1$ satellite changes smoothly with increasing temperature in the lock-in range, displays a slope change at T_{ic}, and is detectable up to T_N (figure 4(a)). The peak shape of this reflection shows a pronounced asymmetry towards low angles down to 8 K. We tentatively deconvoluted the $\{1, 1, 0\}$-$\boldsymbol{q}_1$ peak assuming two peaks with the same half-width in figure 4(a). The behaviour of the weak peak, denoted by Int (?) resembles that of the zero-point satellite. This suggests the presence of a coexisting phase. Higher harmonics like $3\boldsymbol{q}_i, 5\boldsymbol{q}_i$ expected to occur in modulated structures can be ruled out because of the different 2θ position. The eventual presence of a further wavevector, i.e. (0, 0, 1/3), or short-range order effects, needs to be detected by single-crystal data not presently available as it cannot be confirmed from a single observation in the powder patterns.

The temperature variation of the $\boldsymbol{q}_2$ intensities (figure 4(b)) shows that all satellites appear below 42 ± 1 K, in agreement with the magnetic measurements, and that they display a small discontinuity and slope change at T_{ic}.

3.1.3. Thermal behaviour of two unidentified reflections. Figure 4(c) shows that the two unidentified weak peaks ($\mathbf{i}_1$ and $\mathbf{i}_2$, see section 3.1.1) appear abruptly below 43 K like a first-order transition. Given the fact that their 2θ positions do not vary with temperature they

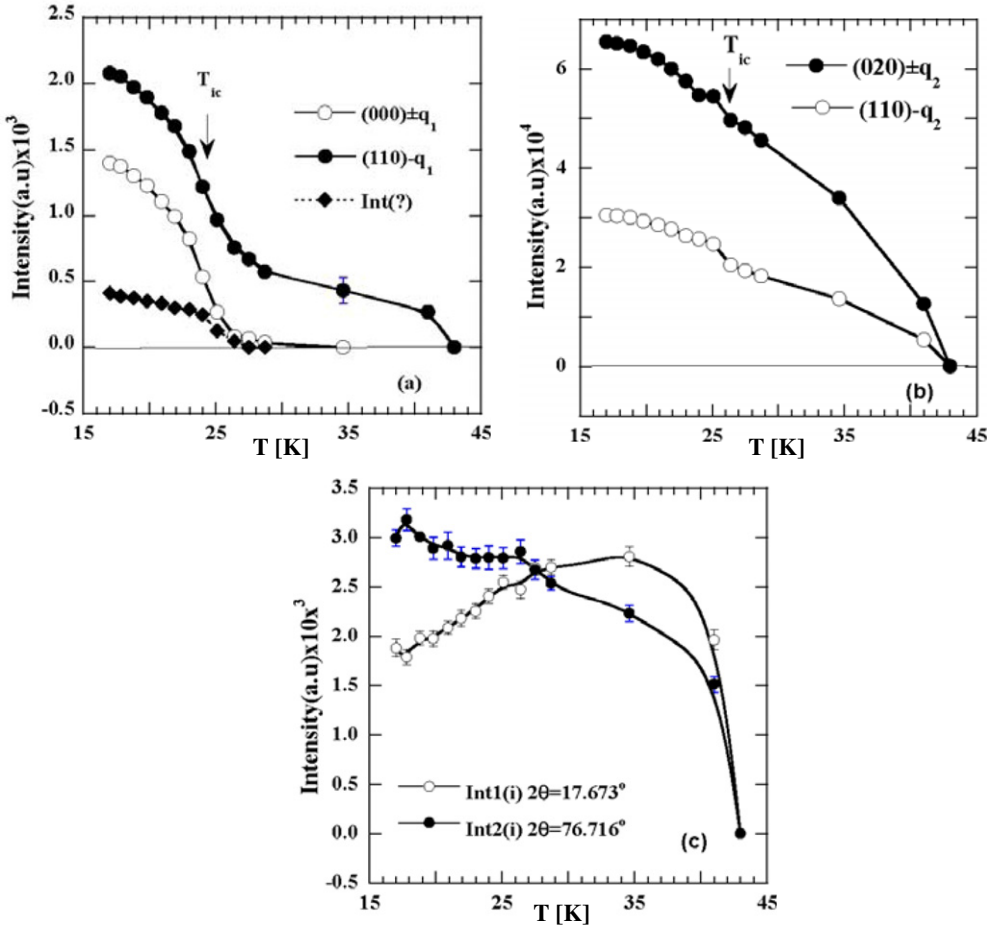

Figure 4. Thermal variation of the integrated magnetic intensities of various magnetic satellites pertaining to the wavevectors: (a) $\boldsymbol{q}_1 = (q_{1x}, 0, 0)$, (b) $\boldsymbol{q}_2 = (q_{2x}, 0, q_{2z})$ of $TbGe_3$. Also shown is the different behaviour of the integrated intensities of two unidentified weak reflections appearing below T_N.

cannot be considered as higher harmonics of the incommensurate magnetic phase. If they are of magnetic origin they should pertain to a third wavevector of $TbGe_3$ which does not show temperature dependence. Contributions from the known neighbour phases $TbGe_2$ (T_N = 41 K) [6] and Tb_3Ge_5 (T_N = 17 K) [7] can be ruled out: the former because of the peak position, and the latter because of the ordering temperature. Therefore they most likely arise from the ordering of a small amount of a novel coexisting Tb–Ge phase with similar ordering temperature. Venturini [8] reports the existence of two new $ErGe_{3-x}$ compounds of composition Er_2Ge_5 and $ErGe_{1.16}$. We suggest that isomorphic compounds could also be present in the Tb–Ge system, and these will be investigated in the future.

3.2. The magnetic phase diagram

The above experimental observations are model independent (profile matching) and are summarized in a magnetic phase diagram in figure 5(a) that will be followed to trace our data analysis in the next sections. The magnetic order is fully described by the symmetry-

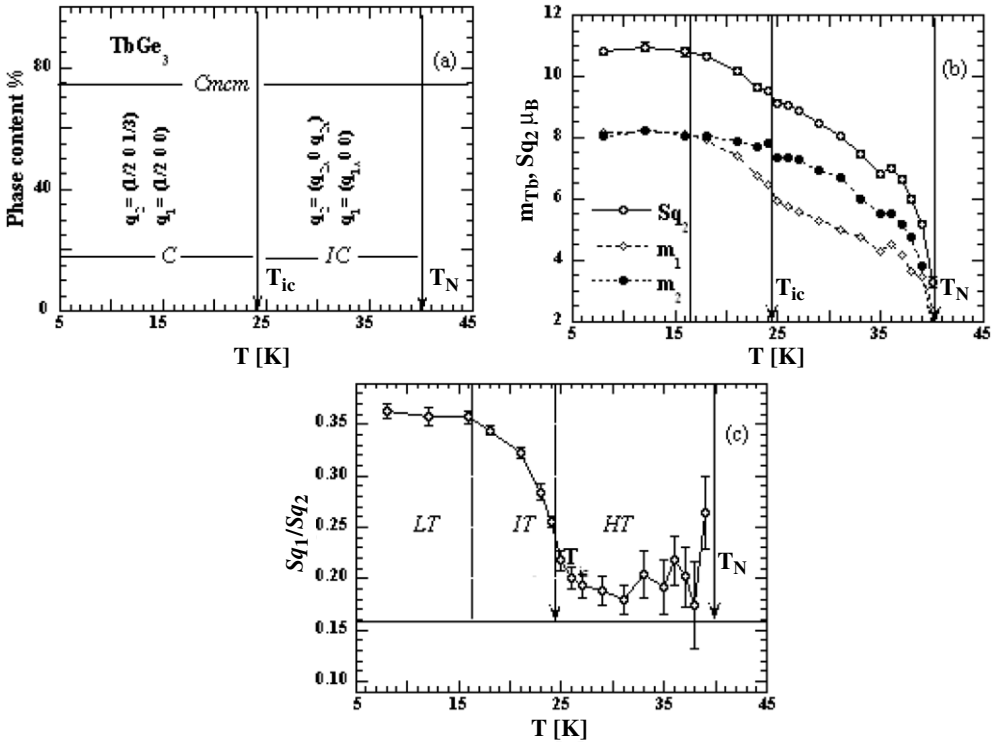

Figure 5. The magnetic phase diagram of $TbGe_3$: from the G6 data (profile matching) (a), from the refinements of the DMC data in terms of Fourier analysis (b) the Tb magnetic moments $\boldsymbol{\mu}_1$ and $\boldsymbol{\mu}_2$ ($\boldsymbol{\mu}_1 = \boldsymbol{m}_1 = \boldsymbol{m}_2$ and $\boldsymbol{\mu}_2 = \boldsymbol{m}_0$ cf equation (1)) versus T, and (c) the Fourier components $\boldsymbol{S}_1(\mathbf{q}_2)$ (amplitude of Tb atom $1''$ in figure 8(a)) and of the ratio $|\boldsymbol{S}_1(\boldsymbol{q}_1)|/|\boldsymbol{S}_1(\boldsymbol{q}_2)|$ versus T.

independent wavevectors $\boldsymbol{q}_1$ and $\boldsymbol{q}_2$. This set of vectors describes several observed magnetic peaks at any temperature of $TbGe_3$. No higher harmonics are observed, nor any symmetry lowering. The phase diagram comprises three distinct ranges of magnetic order. The first is the paramagnetic range for $T > T_N$. The second is the HT range, from T_N down to T_{ic}, where both vectors (i) are incommensurate (IC) with the crystal lattice $\boldsymbol{q}_1 = (q_{1x}, 0, 0)$, $\boldsymbol{q}_2 = (q_{2x}, 0, q_{2y})$ with $q_{1x} \neq q_{2x}$ and (ii) display different thermal behaviour. Finally, there is the lock-in range (C)T_{ic} down to 8 K, where the vectors lock in to the values $\boldsymbol{q}_1 = (1/2, 0, 0)$ $\boldsymbol{q}_2 = (1/2, 0, 1/3)$. Further details concerning the nature of the squaring up of the modulated lock-in structure are obtained from the data analysis that follows in section 5.3 (see figures 5(b) and (c)).

4. Refinements of crystal and magnetic structures

The magnetic refinements were carried out for a full data set (DMC instrument); however, we present only four characteristic refinements representative of the three stability ranges of the magnetic phase diagram given in figure 5(a). The most important parameters with regard to the magnetic ordering obtained from the other data are summarized in figures 5(b) and (c) and will be discussed in detail. For the C-range we present the results of two refinements: one at 8 K, the lowest measured temperature, and the second at 23 K, the upper stability border of the commensurate phase. Figure 6 shows the 8 K refinement together with that at 60 K in the paramagnetic state. The 23 K refinement is compared with that at 25 K just above the $C \rightarrow IC$

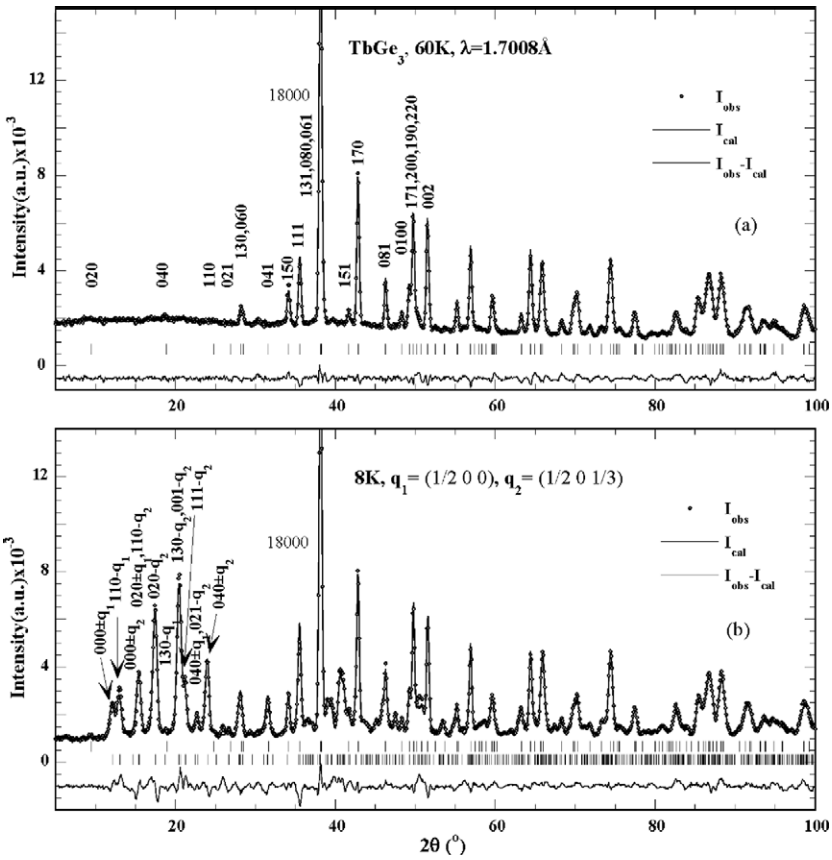

Figure 6. A part of the observed and calculated neutron diffraction patterns of $TbGe_3$: (a) in the paramagnetic state at 60 K, and (b) in the lock-in magnetically ordered state (LT) at 8 K with $q_1 = (1/2, 0, 0)$ and $q_2 = (1/2, 0, 1/3)$ referring to the C-cell.

transition in figure 7. The three unexplained weak observations (peak overlapping with satellite $\{1, 1, 0\}$-q_1 and the $\mathbf{i}_1$, $\mathbf{i}_2$ impurity lines) are excluded throughout our refinements as they would not strongly affect the results.

The strongest magnetic reflections are concentrated in the low-angle part at all temperatures. The main changes with increasing temperature are not in the peak topology, which does not change drastically, but rather in the decrease of relative intensities. The largest changes between the C and IC structures are marked by arrows in figure 7(b) for two data sets at either side of the T_{ic} transition. The refinements at any temperature are based on the magnetic model described in section 5. Table 1 summarizes the refined structural parameters obtained at various temperatures.

4.1. The revised commensurate 8 K refinement

Table 2 refers to the revised 8 K refinement in the C approximation with the Shubnikov model [1]. In this refinement the background was refined and the scale factor was fixed to the value of the 60 K structural refinement due to strong correlations with the moment values. The present results lead to a uniaxial model with all moments confined to the shortest crystal

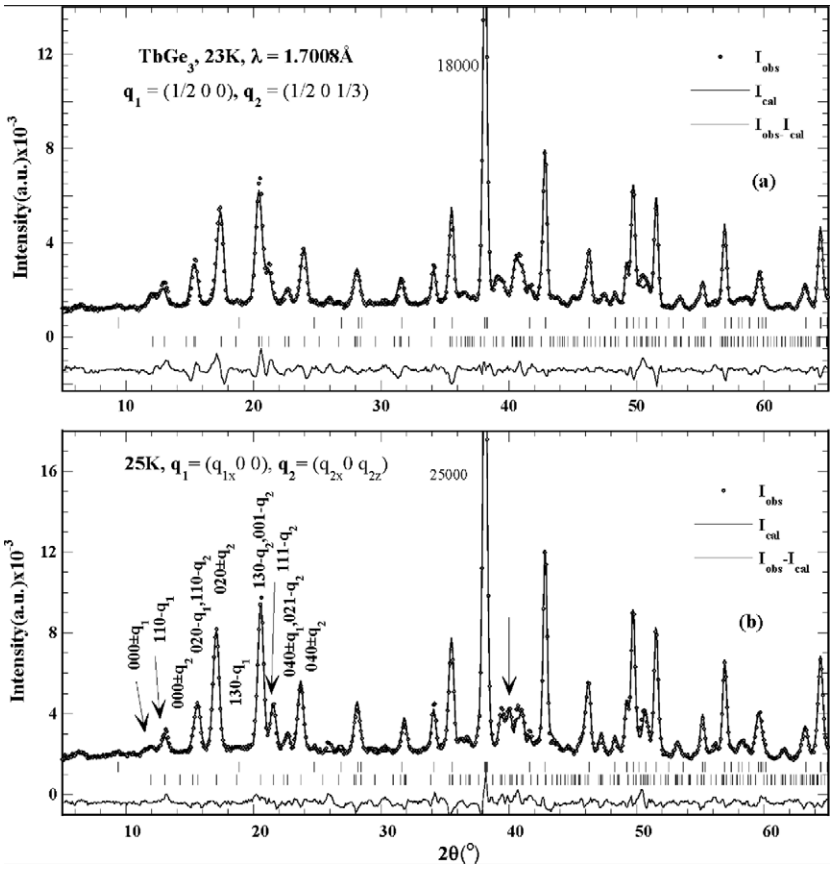

Figure 7. A part of the observed and calculated neutron diffraction patterns of $TbGe_3$: (a) in the lock-in magnetically ordered state (LT) at 23 K state, and (b) in the (HT) incommensurate state at 25 K.

Table 1. Refined structural parameters of $TbGe_3$ from neutron diffraction data: (i) in the paramagnetic state at 60 K, and (ii) the magnetically ordered state (8 K, 23 K and 25 K). Space group $Cmcm$ (No. 63); all atoms at 4c: (0, y, 1/4).

Atom	60 K		8 K	23 K	25 K
	x	y	y	y	y
Tb	0.0	0.4164(2)	0.4167(2)	0.4170(3)	0.4167(2)
Ge(1)	0.0	0.0392(2)	0.0382(2)	0.0392(3)	0.0394(2)
Ge(2)	0.5	0.1921(2)	0.1917(2)	0.1911(3)	0.1918(2)
Ge(3)	0.5	0.3096(2)	0.3095(2)	0.3093(9)	0.3095(3)
B (Å)^2	0.53(7)		0.61(4)	0.61(9)	0.54(14)
a (Å)	4.0473(1)		4.0470(2)	4.0456(3)	4.0446(3)
b (Å)	20.7965(8)		20.804(1)	20.793(2)	20.786(1)
c (Å)	3.9162(1)		3.9148(2)	3.9332(3)	3.9126(3)
R_B, R_{wp}, R_{exp}%, χ^2:		6, 13, 7, 3.7	6, 13.7, 5, 8	5, 15, 5, 9	4.3, 11.6, 4, 8

axis c. The small moment deviation of 6.8° from the c-axis towards b of atoms at the 8f site reported in [1] could not be confirmed. The magnetic moment values 8.15(7) μ_B for Tb1 and

Table 2. Coordinates and magnetic modes of the 4*c* and 8*f* Tb sites in the magnetic space group $P_a mcm$ or $P_b mma$ (Sh_{51}^{299}) [3]. Atoms shifted by (1/2, 0, 0) have opposite signs. Also given are the 8 K refined moment values shown in figure 8(b). The atom labels refer to figure 8(a) (*IC* model). (Note: The magnetic reliability factor of this refinement is $R_m = 8.7\%$.)

4*c* site							
x	y	z			F_z	Atom number	$\mu_z[\mu_B]$
0	y	1/4			+	2	−8.15(7)
0	$-y$	3/4			+	1″	−8.15(7)
8*f* site							
x	y	z	A_x	A_y	F_z	Atom number	$\mu_z[\mu_B]$
0	y	z	+	+	+	1	8.30(5)
0	$-y$	$1/2+z$	−	−	+	2′	8.30(5)
0	y	$1/2-z$	−	−	+	1′	8.30(5)
0	$-y$	$-z$	+	+	+	2″	8.30(5)

8.30(5) μ_B for Tb2 are within error mutually equal and inferior to those in [1], and they are lower than the Tb^{3+} free-ion value $gJ\mu_B = 9\ \mu_B$, most likely because of crystalline field effects. The reliability factors R_B, R_m, R_{wp}, R_{exp} and χ^2: 5.8%, 8.8%, 14%, 5%, 8 are lower than in [1] and comparable with the results for the *IC* approximation given in the last column of table 3 at 8 K. In table 3 we summarize the refined magnetic parameters for the *C* range (8 K, 23 K) and the *HT* range (25 K) in the *IC* approximation using the model developed below. The refined commensurate magnetic structure at 8 K is shown in figure 8(b). It corresponds to a uniaxial antiphase domain moment arrangement with one amplitude with the moment sequence (+−−) along *c* and (+−) along *a*. The atoms related by the $t_C = [1/2, 1/2, 0]$ translation have their moments in opposite directions. This together with the anti-translation (1/2, 0, 0) results in the arrangement (+−− + +−− ...) along the [1, 1, 0] diagonal.

4.2. Symmetry in incommensurate systems

Symmetry considerations provide parameter constraints and are a valuable help in the refinements of complex incommensurate magnetic structures such as the magnetic ordering of $TbGe_3$ with the vectors $\boldsymbol{q}_1 = (q_{1x}, 0, 0)$ and $\boldsymbol{q}_2 = (q_{2x}, 0, q_{2y})$. Such structures may be described in various equivalent ways, i.e. analysis in terms of irreducible representations, by magnetic superspace groups, or by generalized Shubnikov groups.

Our analysis given in the appendix is based on the first way. The results summarized in tables 4 and 5 for the $\boldsymbol{q}_1$ and $\boldsymbol{q}_2$ vectors respectively provide the basis functions and signs of the Fourier components of the magnetic atoms at 4*c* Tb1: (0, *y*, 1/4) and Tb2: (0, −*y*, −1/4) atoms in our calculations. For the wavevector $\boldsymbol{q}_1$, i.e. symmetry analysis results to either uniaxial moment arrangements $F_z(++)$ or $A_z(+-)$ along *c* or planar $F_x A_y$, $A_x F_y$. For the $\boldsymbol{q}_2$ wavevector the situation is more complex; see the next section and the appendix.

5. Equivalence of the models refined in the *C* and *IC* approximations at 8 K

5.1. The IC approximation

The *IC* refinements use the basis functions of the Irreps for the 4*c* site given in tables 4 and 5 for the wavevectors $\boldsymbol{q}_1 = (q_{1x}, 0, 0)$ and $\boldsymbol{q}_2 = (q_{2x}, 0, q_{2z})$ respectively. In the lock-in state

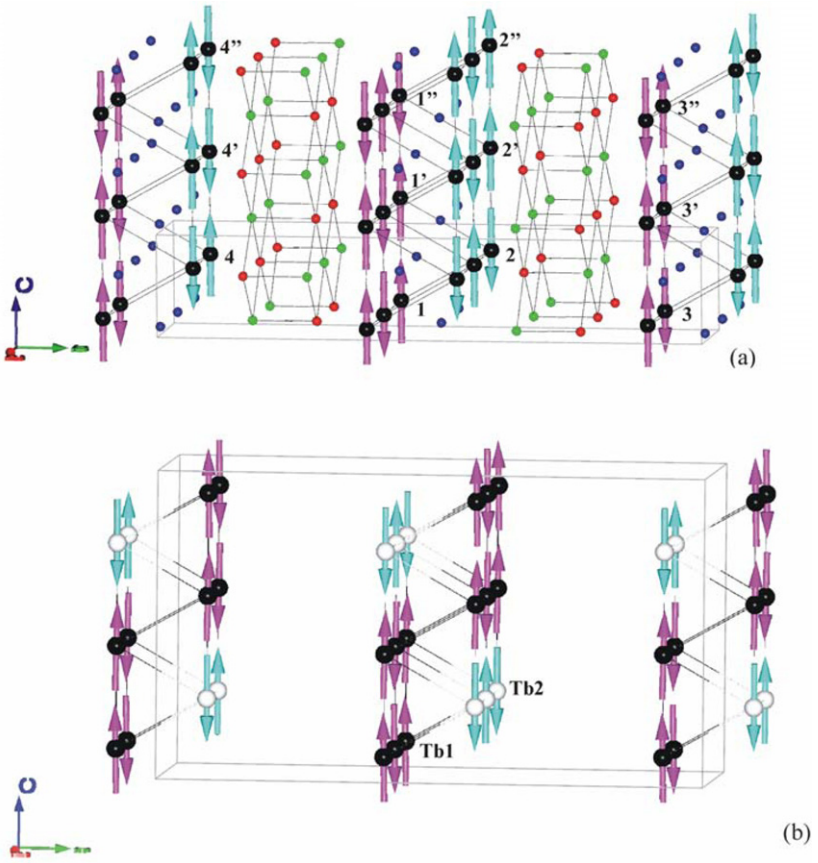

Figure 8. The uniaxial lock-in LT magnetic structure from refinements in the IC (a) and C (b) approximation of $TbGe_3$ at 8 K. In the latter only the Tb atoms are shown.

range the best fit was obtained for uniaxial structures with the moments confined to the c-axis for both vectors. Both magnetic moment arrangements are described by a single representation. For $\boldsymbol{q}_1$ we find Γ_4 with the Tb1 and Tb2 moments parallel ($F_z(++)$ mode). For $\boldsymbol{q}_2$ we found Γ_1 with the $A_z(+-)$ mode. A_z means here $S1z$–$bS2z$. According to equation (4) for this arrangement the Tb moments are also parallel (F_z mode). Because of the special wavevector value $q_{2z} = 1/3$ the Tb2 Fourier coefficient is multiplied by the phase factor $b = \mathrm{e}^{-3\pi \mathrm{i} q_z} = -1$, resulting in a phase inversion.

Both $\boldsymbol{q}_1, \boldsymbol{q}_2$ magnetic structures result in sinusoidal modulated structures. At 8 K the refined Fourier coefficients are 3.92 μ_B for $\boldsymbol{q}_1$ and 10.8 μ_B for $\boldsymbol{q}_2$ (table 3). The real structure for each independent system may be derived by Fourier expansion from the refined Fourier coefficients $\boldsymbol{S}_\nu(\boldsymbol{q}_j)$ of the magnetic moments in the basic unit cell (table 3) using expression (1).

The Fourier expansion of any periodic magnetic moment arrangement with the moments at positions $\boldsymbol{R}_{n\nu} = \boldsymbol{r}_\nu + \boldsymbol{R}_n$, where $\boldsymbol{R}_n = n_1\boldsymbol{a} + n_2\boldsymbol{b} + n_3\boldsymbol{c}$ is a lattice translation vector with n_3 always integer and (n_1, n_2) integer or simultaneously half integers (because the lattice is C-centred), and $\boldsymbol{r}_\nu$ is the vector position of the atom ν in a primitive unit cell (in our case $\nu = 1, 2$), can be expressed by the formula

Table 3. Refined magnetic moment amplitudes (Fourier coefficients for $\boldsymbol{q}_1$ and $\boldsymbol{q}_2$) phases φ and total phases Φ_T for Tb1 at (0, y, 1/4) and Tb2 at (0, $-y$, 3/4) in the LT (8 K and 23 K) and HT (25 K) neutron data of $TbGe_3$. Tb3 and Tb4 atoms shifted by (1/2, 1/2, 0) have the same moment values but opposite signs at LT. R_m% is the agreement factor for the magnetic refinements. (Note: φ is the phase between Fourier components of magnetic moments of the same representation in the commensurate refinement fixed by symmetry. $\Phi_T = \varphi(\boldsymbol{q}_i) + \Psi_G \cdot \Psi_G$ are global phases (origin shift) of a given arrangement, obtained by optimization.)

Atom	R_m %	$\varphi(\boldsymbol{q}_1)$/ $\varphi(\boldsymbol{q}_2)$	$S_y(\boldsymbol{q}_j)$ [μ_B]	$S_z(\boldsymbol{q}_j)$ [μ_B]	$\lvert\boldsymbol{S}(\boldsymbol{q}_j)\rvert$ [μ_B]	Φ_T	μ_y [μ_B]	μ_z [μ_B]	Atom number figure 8(a)	μ_T [μ_B]
8 (K)	8.7									
Tb1($\boldsymbol{q}_1$)		0		3.92(6)	3.92(6)	$\pi/4$		2.77(4)	1, 1′	8.17(5)
Tb1($\boldsymbol{q}_2$)		0		10.8(1)	10.8(1)	$-\pi/3$		5.4(5)	1″	−8.03(5)
Tb2($\boldsymbol{q}_1$)		0		3.92(6)	3.92(6)	$\pi/4$		2.77(4)	2	−8.03(5)
Tb2($\boldsymbol{q}_2$)		$4\pi/3$		10.8(1)	10.8(1)	π		−10.8(1)	2′, 2″	8.17(5)
23 K	8.8									
Tb1($\boldsymbol{q}_1$)		0		2.7(1)	2.7(1)	$\pi/4$		1.9(1)	1, 1′	6.7(1)
Tb1($\boldsymbol{q}_2$)		0		9.6(1)	9.6(1)	$-\pi/3$		4.8(1)	1″	−7.7(1)
Tb2($\boldsymbol{q}_1$)		0		2.7(1)	2.7(1)	$\pi/4$		1.9(1)	2	−7.7(1)
Tb2($\boldsymbol{q}_2$)		$4\pi/3$		9.6(1)	9.6(1)	π		−9.6(1)	2′, 2″	6.7(1)
25 (K)	11.6								Figure 9	
Tb1($\boldsymbol{q}_1$)		0		2.0(1)	2.0(1)	$\pi/4$		1.4(1)	1	5.9(1)
Tb1($\boldsymbol{q}_2$)		0	3.1(3)	−8.6(1)	9.14(7)	$\pi/3$	1.5(1)	−4.3(1)	1′	8.51
									1″	4.47
Tb2($\boldsymbol{q}_1$)		0		1.5(3)	2.0(1)	$\pi/4$	0.90	−1.06	2	5.7
Tb2($\boldsymbol{q}_2$)		$4\pi/3$	3.1(3)	8.6(1)	9.14(7)	$2\pi/3$	−1.7	−4.6	2′	5.4
									2″	8.52

Table 4. Irreducible representations and magnetic modes for $\boldsymbol{q}_1 = (q_x, 0, 0)$ in $Cmcm$.

Irrep	(1|0)	$(2_x\|0)$	$(m_y\|001/2)$	$(m_z\|001/2)$	x	y	z
Γ_1	1	1	1	1	0	0	A_z
Γ_2	1	1	−1	−1	F_x	A_y	0
Γ_3	1	−1	1	−1	A_x	F_y	0
Γ_4	1	−1	−1	1	0	0	F_z
Atom							
1	1	2	2[001]	1[001/2]	<= Permutation of atoms		
2	2	1	1	2[001]	and 'returning' translations		

$$\boldsymbol{m}_v(\boldsymbol{R}_n) = \sum_{\{j\}} \boldsymbol{S}_v(\boldsymbol{q}_j) \exp(-2\pi \mathrm{i} \boldsymbol{q}_j \cdot \boldsymbol{R}_n) = \sum_j \boldsymbol{S}_v^R(\boldsymbol{q}_j) \cos\{2\pi \boldsymbol{q}_j \cdot \boldsymbol{R}_n + \varphi_{jv}\}. \quad (1)$$

The first sum is extended for all pairs $(\mathbf{q}_j, -\boldsymbol{q}_j)$ of propagation vectors; in the second one we have assumed that the Fourier coefficients have the form $\boldsymbol{S}_v(\boldsymbol{q}_j) = 1/2\boldsymbol{S}_v^R(\boldsymbol{q}_j)\mathrm{e}^{-\mathrm{i}\varphi_{jv}}$ so that only cosine terms appear after grouping the pairs $(\boldsymbol{q}_j, -\boldsymbol{q}_j)$. Only two sets of magnetic satellites $(\boldsymbol{H} \pm \boldsymbol{q}_j)$ of the wavevectors $\boldsymbol{q}_1$ and $\boldsymbol{q}_2$ are observed as (1/2, 0, 0) is an anti-translation. The phases $\varphi_v(\boldsymbol{q}_j) = \varphi_{jv}$ between atoms of the same orbit are deduced by symmetry analysis from the basis functions of the representation. These are usually products of the wavevectors by the translation part of the symmetry operators of G_q and/or returning translations. In commensurate phases these are fixed. If there is more than one orbit an additional phase between the orbits has to be refined. In the LT range the phases for $\boldsymbol{q}_1$ are zero, while for $\boldsymbol{q}_2$ Tb2 has a phase of $2/3 \times 2\pi = 4/3\pi$. A commensurate amplitude-modulated structure can

Table 5. Irreducible representations and magnetic modes for $\boldsymbol{q}_2 = (q_{2x}, 0, q_{2z})$ in $Cmcm$.

Irrep	(1|0)	$(m_y\|001/2)$	x	y	z
Γ_1	1	ω^a	A_x	F_y	A_z
Γ_2	1	$-\omega$	F_x	A_y	F_z
Atom					
1	1	2[001]		<= Permutation of atoms	
2	2	1		and 'returning' translations	

$\omega = \exp(-\pi i q_z)$

be transformed, in some circumstances, to a constant-moment phase by adding an appropriate global phase to the origin. In our case, i.e. for $\boldsymbol{q}_1$, the atoms 3 and 4 translated by $[1/2, 1/2, 0]$ have a phase of $2\pi/4$ and therefore zero ordered moment $(\boldsymbol{S}_\nu(\boldsymbol{q}_j)\cos\pi/2)$, while the amplitude of the moments of Tb1 and Tb2 are 3.92 μ_B. An origin shift by inserting a global phase of $\Psi_G = \pi/4$ results in equal moment values:

$$\boldsymbol{S}_3(\boldsymbol{q}_1)\cos(2\pi/4 + \pi/4) = -\boldsymbol{S}_1(\boldsymbol{q}_1)\sqrt{2}/2 = 2.77\ \mu_B$$

and a sign change of $(++--++--\ldots)$ for atoms translated along the (110) diagonal. For the $\boldsymbol{q}_2$ structure the global phase of $\Psi_G = -\pi/3$ leads to a commensurate structure with two amplitudes 5.4 μ_B for Tb1 and 2×5.4 μ_B for Tb2. The amplitudes of the Fourier coefficients of the $\boldsymbol{q}_1$ magnetic phase are strongly reduced below the free-ion value. Also the two unequal moment values, one being larger than the free-ion value of the $\boldsymbol{q}_2$ structure, are not convincing. In principle the $\boldsymbol{q}_1, \boldsymbol{q}_2$ Fourier coefficients describe two independent magnetic systems coexisting in the form of domains. Alternatively one may assume that the two wavevectors act on the same physical space. In this case the real structure has to be derived by equation (1) by adding up all observed Fourier coefficients, as explained in the next section.

*5.2. The lock-in multiple **q**-vector commensurate structure*

In general the Fourier coefficients $\boldsymbol{S}_\nu(\boldsymbol{q}_j)$ [9] are complex vectors with six components and the phase between them cannot be found by diffraction as there is no information about the relative phases between reflections of independent wavevectors. This is a general problem of diffraction of multiple ***q**-vector* structures. By a proper choice of the global phase(s) Ψ_G one may obtain equal moment values in special cases or at least minimize the fluctuations of the resulting moment values. A shift of the origin of the wave in IC phases does not affect the magnetic refinements. If the magnetic transition succeeds over more than one branch of the same wavevector star there exist several theoretical methods to deduce the ordered magnetic moment value in the commensurate range [10–12]. In our case with two symmetry-independent vectors the problem may be solved using the program 'Moment' [13], which makes a phase optimization for minimizing the fluctuation of the moment values.

Figure 8 compares the 8 K magnetic structures obtained from refinements using the incommensurate (IC, top part) and the commensurate (C, lower part) formalism. The IC model spans $2a, 3c$ cells. In the C model only the magnetic atoms are shown.

The moments of the 24 atoms in the $2a, 3c$ enlarged magnetic unit cell are indicated by $\boldsymbol{m}_0, \boldsymbol{m}_1, \boldsymbol{m}_2$ for the atoms $\boldsymbol{r}_\nu, \boldsymbol{r}_\nu + \boldsymbol{c}, \boldsymbol{r}_\nu + 2\boldsymbol{c}$, by $-\boldsymbol{m}_0, -\boldsymbol{m}_1, -\boldsymbol{m}_2$ for those at $\boldsymbol{r}_\nu + \boldsymbol{a}, \boldsymbol{r}_\nu + \boldsymbol{a} + \boldsymbol{c}, \boldsymbol{r}_\nu + \boldsymbol{a} + 2\boldsymbol{c}$ for $\nu = 1$ and by $\pm\boldsymbol{m}'_j$ for $\nu = 2$. Atoms 3 and 4, related by the $\boldsymbol{t}_C = [1/2, 1/2, 0]$ translation to 1 and 2, have a phase of $\boldsymbol{q}_j \cdot \boldsymbol{t}_C$. The moment arrangement along the chains $\boldsymbol{r}_{n2}$ and $\boldsymbol{r}_{n3}$ corresponds to a shift by $2/3\boldsymbol{c}$ to that of chains $\boldsymbol{r}_{n1}$ and $\boldsymbol{r}_{n4}$.

In the LT range the vectors $\boldsymbol{S}_\nu(\boldsymbol{q}_j)$ are all along $\boldsymbol{c}$; therefore the moments are also along the unit vector along $\boldsymbol{c}$, denoted hereafter as $\hat{z}$. Then the moments of the νth atom in the nth

cell $\boldsymbol{m}_\nu(\boldsymbol{R}_n)$ can be found by rewriting formula (1) for the vectors $\boldsymbol{S}_\nu \boldsymbol{q}_j$ and the total phase given in table 3:

$$\boldsymbol{m}_\nu(R_n) = \boldsymbol{S}_\nu(\boldsymbol{q}_1)\cos(2\pi \boldsymbol{q}_1 \cdot \boldsymbol{R}_n + \Phi_{T_\nu}) + \boldsymbol{S}_\nu(\boldsymbol{q}_2)\cos(2\pi \boldsymbol{q}_2 \cdot \boldsymbol{R}_n + \Phi_{T_\nu}). \tag{2}$$

For Tb1 ($\nu = 1$) this gives the distribution

$$\begin{aligned}\boldsymbol{m}_0 &= \boldsymbol{S}_1(\boldsymbol{q}_1)\cos(\pi/4) + \boldsymbol{S}_1(\boldsymbol{q}_2)\cos(-\pi/3)\\ &= \boldsymbol{S}_1(\boldsymbol{q}_1)\sqrt{2}/2 + \boldsymbol{S}_1(\boldsymbol{q}_2)/2 = 8.17\ \mu_B\hat{z} \qquad (3a)\\ \boldsymbol{m}_1 &= \boldsymbol{S}_1(\boldsymbol{q}_1)\cos(\pi/4) + \boldsymbol{S}_1(\boldsymbol{q}_2)\cos(2\pi/3 - \pi/3)\\ &= \boldsymbol{S}_1(\boldsymbol{q}_1)\sqrt{2}/2 + \boldsymbol{S}_1(\boldsymbol{q}_2)/2 = 8.17\ \mu_B\hat{z} \qquad (3b)\\ \boldsymbol{m}_2 &= \boldsymbol{S}_1(\boldsymbol{q}_1)\cos(\pi/4) + \boldsymbol{S}_1(\boldsymbol{q}_2)\cos(4\pi/3 - \pi/3)\\ &= \boldsymbol{S}_1(\boldsymbol{q}_1)\sqrt{2}/2 - \boldsymbol{S}_1(\boldsymbol{q}_2) = -8.03\ \mu_B\hat{z}. \qquad (3c)\end{aligned}$$

For Tb2($\nu = 2$)

$$\begin{aligned}\boldsymbol{m}'_0 &= \boldsymbol{S}_2(\boldsymbol{q}_1)\cos(\pi/4) + \boldsymbol{S}_2(\boldsymbol{q}_2)\cos(\pi)\\ &= \boldsymbol{S}_2(\boldsymbol{q}_1)\sqrt{2}/2 - \boldsymbol{S}_2(\boldsymbol{q}_2) = -8.03\ \mu_B\hat{z} \qquad (3d)\\ \boldsymbol{m}'_1 &= \boldsymbol{S}_2(\boldsymbol{q}_1)\cos(\pi/4) + \boldsymbol{S}_2(\boldsymbol{q}_2)\cos(5\pi/3)\\ &= \boldsymbol{S}_2(\boldsymbol{q}_1)\sqrt{2}/2 + \boldsymbol{S}_2(\boldsymbol{q}_2)/2 = 8.17\ \mu_B\hat{z} \qquad (3e)\\ \boldsymbol{m}'_2 &= \boldsymbol{S}_2(\boldsymbol{q}_1)\cos(\pi/4) + \boldsymbol{S}_2(\boldsymbol{q}_2)\cos(7\pi/3)\\ &= \boldsymbol{S}_2(\boldsymbol{q}_1)\sqrt{2}/2 + \boldsymbol{S}_2(\boldsymbol{q}_2)/2 = 8.17\ \mu_B\hat{z}. \qquad (3f)\end{aligned}$$

The resulting magnetic moment values 8.17(5) μ_B and 8.03(5) μ_B for Tb1 and Tb2 respectively (last column of table 3) are within error identical to those of the *C* approximation 8.30(5) μ_B and 8.15(7) μ_B (table 2) for the atoms Tb1 at 8*f* and Tb2 at 4*c* sites respectively. The reliability factors of the two refinements are comparable.

5.3. The squaring up of the lock-in structure

Figure 5(b) shows that the magnetic moments of the two Tb sites display a different thermal variation. In the 8–16 K range the magnetic moments remain unchanged. Above 16 K one observes a strong decrease of the Tb1 (m_1) moment values that change by 25% in the range 16–24 K, while Tb2 ($\boldsymbol{m}_2$) changes more smoothly and decreases by only 5% in the same range. This strange behaviour may be better described in terms of Fourier coefficients. In the *C* range the magnetic ordering is described by one harmonic of each wavevector; however, the ratio of the Fourier coefficients $|\boldsymbol{S}(\boldsymbol{q}_1)|/|\boldsymbol{S}(\boldsymbol{q}_2)|$ is temperature dependent. Figures 5(b) and (c) show that the *C* range has two distinct ranges depending on the $|\boldsymbol{S}(\boldsymbol{q}_1)|/|\boldsymbol{S}(\boldsymbol{q}_2)|$ ratio. In the *LT* range (8–16 K) where the $|\boldsymbol{S}(\boldsymbol{q}_1)|/|\boldsymbol{S}(\boldsymbol{q}_2)|$ is fixed. In this range equations (3*a*)–(3*c*) result in the expressions

$$\boldsymbol{S}_1(\boldsymbol{q}_1) = \sqrt{2}\frac{\boldsymbol{m}_0 + \boldsymbol{m}_1 + \boldsymbol{m}_2}{3}, \qquad \boldsymbol{S}_1(\boldsymbol{q}_2) = 2\frac{2\boldsymbol{m}_0 - \boldsymbol{m}_1 - \boldsymbol{m}_2}{3}. \tag{4}$$

Along the chain $\nu = 1$ the moment arrangement $(++-)$ obtained by our refinements leads to the $\boldsymbol{S}_1(\boldsymbol{q}_1) = \frac{\sqrt{2}m_0}{3} = \frac{\sqrt{2}m}{3}$, $\boldsymbol{S}_1(\boldsymbol{q}_2) = \frac{4m_0}{3} = \frac{4m}{3}$ values and to the $|\boldsymbol{S}(\boldsymbol{q}_1)|/|\boldsymbol{S}(\boldsymbol{q}_2)| = 0.25\sqrt{2} = 0.353$ ratio, in good agreement with figure 5(c). The magnetic structure of the *LT* range corresponds, within error, to an antiphase domain structure with one amplitude or to a constant-moment structure. In the intermediate *IT* range 24–16 K the ratio $|\boldsymbol{S}(\boldsymbol{q}_1)|/|\boldsymbol{S}(\boldsymbol{q}_2)|$ increases from 0.1909 at 23 K to 0.353 at 16 K. In this range the antiphase domain arrangement remains uniaxial but it is described by two amplitudes:

$$\boldsymbol{m}_0 = \boldsymbol{m}_1 = (\sqrt{2}\boldsymbol{S}(\boldsymbol{q}_1) + \boldsymbol{S}(\boldsymbol{q}_2))/2, \qquad \boldsymbol{m}_2 = (\sqrt{2}\boldsymbol{S}(\boldsymbol{q}_1) - 2\boldsymbol{S}(\boldsymbol{q}_2))/2 \tag{5a}$$

$$\frac{|\boldsymbol{m}_0|}{|\boldsymbol{m}_2|} = (\sqrt{2}|\boldsymbol{S}(\boldsymbol{q}_1)|/|\boldsymbol{S}(\boldsymbol{q}_2)| + 1)/(\sqrt{2}|S(\boldsymbol{q}_1)|/|\boldsymbol{S}(\boldsymbol{q}_2)| - 2). \tag{5b}$$

The continuous increase of the ratio $|\boldsymbol{S}(\boldsymbol{q}_1)|/|\boldsymbol{S}(\boldsymbol{q}_2)|$ with temperature in the IT range corresponds to the squaring up of the modulated structure. In this range the $|\boldsymbol{m}_0|/|\boldsymbol{m}_2|$ ratio increases from 0.87 at 23 K to 1 at 16 K, where it reaches saturation.

5.4. The $C(IT) \rightarrow IC(HT)$ phase transition

Our experiments show that in the IC range $T_N > T > 24$ K both wavevectors become incommensurate with the crystal lattice and $q_{1x} \neq q_{2x}$. The wavevectors are not symmetry related and therefore the structure undergoes a further symmetry lowering to monoclinic. The moment values cannot be compared as their amplitudes vary with their position between 2 and 8 μ_B, and their orientation also changes. The values above 24 K given in figure 5(b) are derived by optimizing the phases between the Fourier coefficients found from the IC approximation to minimize the moment fluctuation by the program `moment`. These values correspond to the maximum local moment value. The $C(IT) \rightarrow IC(HT)$ transition corresponds to a spin reorientation as the $\boldsymbol{S}(\boldsymbol{q}_2)$ Fourier vectors move away from the c-axis in the plane $(0, y, z)$ while the $\boldsymbol{q}_1$ Fourier components remain along $\boldsymbol{c}$.

5.5. The canted fluctuating IC phase

The best model obtained for the $\boldsymbol{q}_2$ phase in the IC range corresponds to ferromagnetic F_y, $F_z(++--)$ arrangements within the cell. The appearance of an F_y mode indicates a further symmetry lowering as the $\boldsymbol{q}_2$ ordering is now described by the combination of two representations $\Gamma_1 + \Gamma_2$ (see table 5). The $\boldsymbol{q}_1$ ordering is described by a single representation Γ_4. The structure itself depends strongly on the phase choice between the Fourier coefficients. The resulting IC structure at any temperature obtained by combining the two Fourier coefficients $\boldsymbol{S}_v(\boldsymbol{q}_1)$ and $\boldsymbol{S}_v(\boldsymbol{q}_2)$ corresponds to a canted periodic arrangement where both the moment amplitude and orientation vary with the position. This is better visible in the plane (0 y z) as the moment direction is slightly fluctuating around the [0, 0, 1] direction. The refined structure at 25 K is shown in figure 9 for a few cells and for a larger range in figure 10. Further details of this ordering become visible in the plane $(x, 0, z)$ containing the $\boldsymbol{q}_1$ and $\boldsymbol{q}_2$ wavevectors for a single atom (figure 11). The moment arrangement of the Tb1 atom along a ($39a \times 13c$ cells) corresponds to an almost transversal modulation in which adjacent Tb atoms have their moments in opposite directions; see figure 11. Along c if one neglects the small μ_y component the arrangement corresponds to $(0+-\ldots 0+-)$ μ_z.

6. Concluding remarks

The $TbGe_3$ lock-in magnetic structure is found to have a uniaxial magnetic moment arrangement in the entire C range 8 K to T_{ic}. Its symmetry is described by the $P_bmma(Sh_{51}^{299})$ Shubnikov space group. We have shown that with a suitable choice of the relative phases between Fourier coefficients the model derived by symmetry analysis with the wavevectors $\boldsymbol{q}_1$ and $\boldsymbol{q}_2$ is equivalent to the commensurate model. The C ordering subdivides in two further regions, not visible in the magnetic measurements, depending on the thermal variation of the ratio $|\boldsymbol{S}(\boldsymbol{q}_1)|/|\boldsymbol{S}(\boldsymbol{q}_2)|$ (Fourier coefficients). In the LT range 8–16 K, $|\boldsymbol{S}(\boldsymbol{q}_1)|/|\boldsymbol{S}(\boldsymbol{q}_2)|$ is fixed to 0.353 and the structure is a constant-moment one. In the IT range 24–16 K,

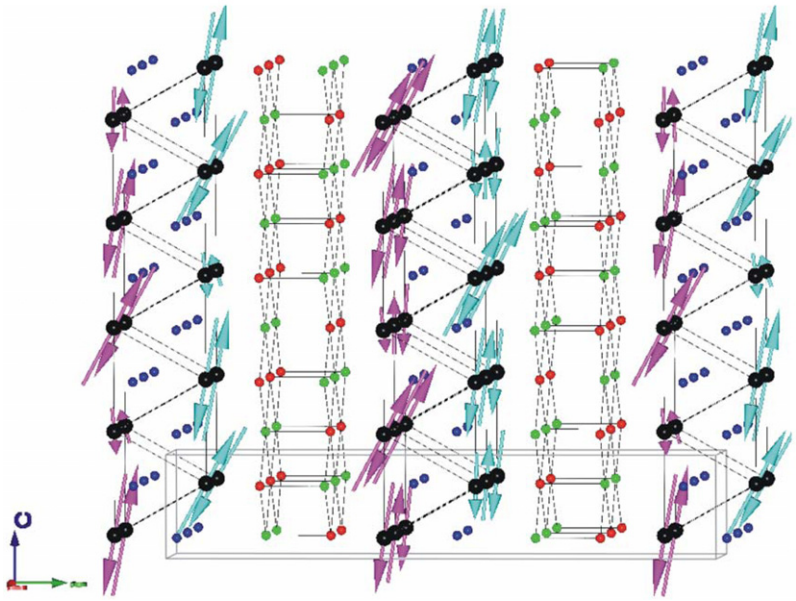

Figure 9. The canted *IC* magnetic structure of $TbGe_3$ at 25 K for a few cells along the *c*-direction. The moment value varies between 2–8 μ_B depending on the position.

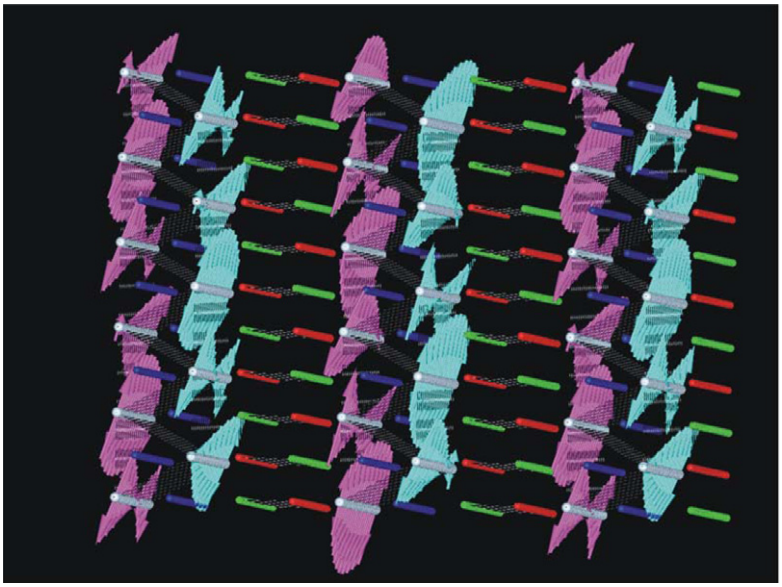

Figure 10. 3D view of the canted *IC* fluctuating magnetic structure of $TbGe_3$ at 25 K for $28 \times a$, $5 \times c$ cells: *c*-axis vertical, *b*-axis horizontal.

the modulated commensurate structure squares up progressively and the ratio $|\boldsymbol{S}(\boldsymbol{q}_1)|/|\boldsymbol{S}(\boldsymbol{q}_2)|$ varies continuously from 0.183 at 24 K to 0.353 at 16 K.

The $(+-)$ arrangement along *a* and the antiphase domain arrangement along $c(+--+--)$ found in the commensurate $TbGe_3$ phase can be explained by antiferromagnetic interactions between (i) the nearest neighbours along the *a* direction (4.01 Å), (ii) next-nearest neighbours along the diagonal $(110)(++--++\ldots)$, and (iii)

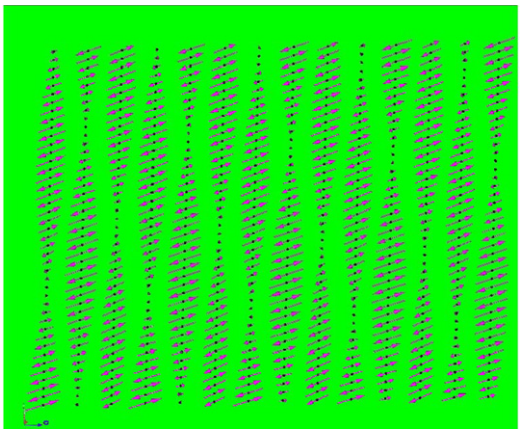

Figure 11. The magnetic moment variation of the Tb1 atom in the (0 1 0) plane containing both wavevectors for $39a \times 13c$ cells. The $\boldsymbol{c}$-axis is horizontal.

ferromagnetic interactions $(+--+--)$ between third-nearest neighbours along the c-axis (3×3.915 Å).

It is interesting to note that the LT two-dimensional (2D) uniaxial $TbGe_3$ magnetic moment arrangements within the $(x, 0, z)$ planes is identical to that obtained for the $DyGe_3$ compound [14]. Both structures have the same easy axis which is the shortest axis c and are described by the wavevectors $\boldsymbol{q}_1 = (1/2, 0, 0)$ and $\boldsymbol{q}_2 = (1/2, 0, 1/3)$ but referring to different basis, P (monoclinic) for $DyGe_3$ and C (orthorhombic) for $TbGe_3$. The canted ordering of the isomorphic $ErGe_3$ compound is described by a single wavevector $\boldsymbol{q} = 0$ [15] and the easy axis is along a. These differences concerning the moment orientation may be explained by assuming that the magnetocrystalline anisotropy in these compounds is crystal-field induced and that the sign of the lowest-order anisotropy constant is determined by the sign of the second-order Stevens factor a_j, which for Er is different from that of Dy and Tb.

The difference between $TbGe_3$ and $DyGe_3$ consists in the stacking of the 2D $(x\ 0\ z)$ magnetic layers perpendicular to the y axis through the non primitive translation $T_C = [1/2\ 1/2\ 0]$ which is ferromagnetic $(++++\ldots)$ for $DyGe_3$ along the (110) diagonal and $(++--\ldots)$ for $TbGe_3$ corresponding to monoclinic and orthorhombic magnetic lattices respectively; see figure 12. The uniaxial moment arrangements observed in both compounds indicate the existence of a strong crystal-field anisotropy that defines the moment orientation. The progressive squaring up of the modulated two-amplitude structure, described by two wavevectors, indicates the existence of competing interactions that are most likely related to the particular Tb geometric arrangement. This geometry consists of blocks of condensed nearly trigonal prisms, with their axis along a and centred by one Ge atom (Ge1), that are separated by Ge double layers (Ge2, Ge3) as shown in figures 8 and 9. Band structure calculations (extended Hückel approach) of the isomorphic $DyGe_3$ [16] which analyse the bonding properties of the Ge1 kinked chains and that of the Ge2 and Ge3 double layers suggest that the layered character of this structure perpendicular to the y axis is associated with a two-dimensional metallic conductivity.

As pointed out by Kimura [17, 18] for the orthorhombic compound $TbCu_2$ showing specific heat anomalies and lock-in transition with $\boldsymbol{q} = 1/3a^*$, the stabilization of the uniaxial lock-in magnetic structure can be described in simple terms as a compromise between the crystal-field anisotropy and competing exchange interactions that lead to similar complex ordering mechanisms.

More complex is the HT ordering of $TbGe_3$ above T_{IC} associated with (i) an incommensurate magnetic phase and the concomitant loss of symmetry and (ii) a spin

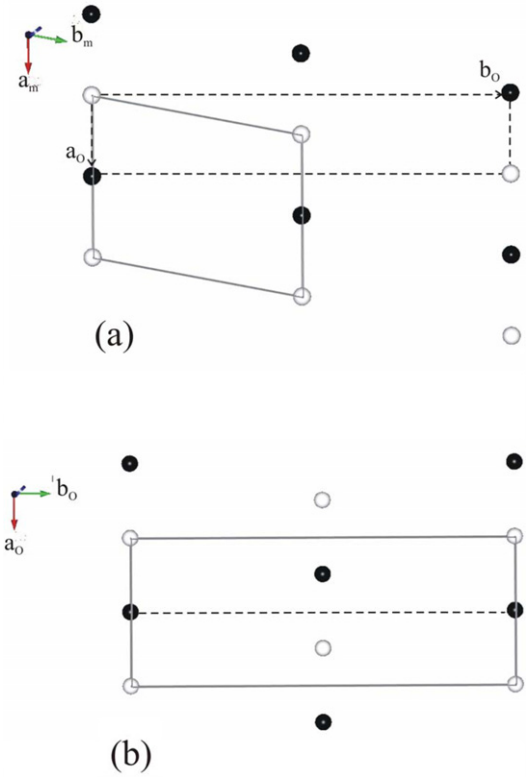

Figure 12. The magnetic lattices of the (a) $DyGe_3$ (monoclinic) and (b) $TbGe_3$ (orthorhombic) commensurate structures viewed along [0, 0, 1]. Filled and open symbols correspond to anti-translation and translation operations respectively.

reorientation transition from a uniaxial modulated magnetic structure with two amplitudes to a canted complex structure. Incommensurate rare earth phases are widely observed at high temperatures due to competition between the *RKKY* long-range exchange interaction mediated via the conduction electrons and the crystal-field anisotropy. The general rule is that they lock in at low temperatures to commensurate structures because of the entropy term in the free energy [9]. The occurrence of canted arrangements as found in $TbGe_3$ may have their origin on various types of mechanisms as the appearance of higher-order terms in the crystalline field or of anisotropic exchange interactions of the Dzyaloshinskii–Moriya type [19, 20]. Kimura [21] found by theoretical calculations based on a 24-sublattice model for the $HoCu_2$ orthorhombic compound that the origin of the spin canting observed at HT was the biquadratic exchange interaction between nearest-neighbouring Ho ions on the adjacent *ac* planes.

6.1. Symmetry

An important result of our analysis is the independence of the q_{1x} and q_{2x} wavevector components in the HT range. Such a structure may also be described by superspace groups or magnetic superspace groups. The structure may have a five-dimensional or six-dimensional superspace group depending on the number of wavevector arms of $\boldsymbol{q}_2$ participating in the magnetic ordering. The wavevector $\boldsymbol{q}_2$ has four arms $(\pm q_{2x}, 0, \pm q_{2z})$, and it could give rise to three independent sets of magnetic satellites if all four arms occur simultaneously, and the rank would be six. If, however, there are domains with $\pm\boldsymbol{q}_2$ or $\pm\boldsymbol{q}_3$, with $\boldsymbol{q}_3 = (-q_{2x}, 0, q_{2z})$ the rank is five, with a monoclinic superspace group. However, this distinction exceeds the limits of powder diffraction. If $q_{1x} = q_{2x}$ the superspace group is five-dimensional but with orthorhombic symmetry, $Cmmm(m1m)$.

Appendix. Symmetry analysis

The magnetic ordering of $TbGe_3$ is characterized by the presence of two propagation vectors:

$$\boldsymbol{q}_1 = (q_{1x}, 0, 0), \qquad \boldsymbol{q}_2 = (q_{2x}, 0, q_{2y}) \qquad \text{with } q_{1x} \approx q_{2x} \approx 1/2 \text{ and } q_{2z} \approx 1/3.$$

The components are given with respect to the reciprocal frame obtained from the conventional basis of the space group $Cmcm$. The magnetic atoms (Tb ions) occupy the positions $4c$ of site symmetry $m2m$:

$$\text{Tb: } 4c\ m2m: \qquad \text{Tb}_1\text{: } (0, y, 1/4) \qquad \text{Tb}_2\text{: } (0, -y, -1/4).$$

For the symmetry analysis it is only necessary to take into account the content of a primitive cell. The two atoms above constitute this content. The atoms 3 and 4 of the conventional unit cell are obtained from (1) and (2) by adding the centring translation $\boldsymbol{t}_C = [1/2, 1/2, 0]$. The propagation vectors $\boldsymbol{q}_1$ and $\boldsymbol{q}_2$ belong to the interior of the Brillouin zone, thus the small representations are obtained easily from the representations of the point groups of the propagation vectors. Symmetry analysis has to be done for each of the wavevectors, as these are symmetry independent, and for all arms of the star(s) separately.

A.1. Propagation vector $\boldsymbol{q}_1$

The point group of $\boldsymbol{q}_1$ is $G_1^0 = 2mm = \{1, 2_x, m_y, m_z\}$, which has four one-dimensional representations. The star of $\boldsymbol{q}_1$ has two arms: $(\boldsymbol{q}_1, -\boldsymbol{q}_1)$. The representations of the space group of $\boldsymbol{q}_1$, $G_1 = C2cm$, are obtained from those of G_1^0 by the expression

$$D^{\gamma}(h|\boldsymbol{t}_h) = \mathrm{e}^{-2\pi \mathrm{i} \boldsymbol{q}\cdot\boldsymbol{t}_h} D^{0\gamma}(h). \tag{A.1}$$

The co-set representatives of G_1 with respect to the translation group are $(1|0)$, $(2_x|0)$, $(m_y|001/2)$, $(m_z|001/2)$. Due to the particular form of the translations the products $\boldsymbol{q}_1\boldsymbol{t}_h$ are zero and the matrices D^{γ} are identical to $D^{0\gamma}$. In table 4 we give the representations and the basis functions corresponding to the Tb site $4c$ and the propagation vector $\boldsymbol{q}_1$.The basis functions $F(++)$ and $A(+-)$ correspond to the signs of the Fourier components $\boldsymbol{S}_{q\nu}$ of the $(\nu = 1, 2)$ atoms Tb_1 and Tb_2. Then, for instance, the Fourier components corresponding to the representation Γ_1 are of the form

$$\boldsymbol{S}_{q_1 1} = (0, 0, a) \quad \text{and} \quad \boldsymbol{S}_{q_1 2} = (0, 0, -a).$$

The same basis functions correspond to the other arm of the star. Thus the magnetic structure corresponds to a modulated structure with the two atoms 1 and 2 in antiphase within the reference cell.

A.2. Propagation vector $\boldsymbol{q}_2$

The point group of $\boldsymbol{q}_2$ is $G_2^0 = 1m1 = \{1, m_y\}$, which has two one-dimensional representations. The star of $\boldsymbol{q}_2$ has four arms:

$$\boldsymbol{q}_2^1 = (q_{2x}, 0, q_{2z}); \qquad \boldsymbol{q}_2^2 = (-q_{2x}, 0, -q_{2z});$$
$$\boldsymbol{q}_2^3 = (-q_{2x}, 0, q_{2z}); \qquad \boldsymbol{q}_2^4 = (q_{2x}, 0, -q_{2z}).$$

The representations of the space group of $\boldsymbol{q}_2$, $G_2 = C1c1$, are obtained from those of G_2^0 by the same expression as above.

The co-set representatives of G_2 are $\tilde{1} = (1|000)$, $\tilde{c}_y = (m_y|001/2)$. Due to the particular form of the translations the products $\boldsymbol{q}_2\boldsymbol{t}_h$ are non-zero and the matrices D^{γ} are not identical to $D^{0\gamma}$. Table 5 gives the representations and the basis functions corresponding to the site $4c$ and the propagation vector $\boldsymbol{q}_2$.

Here the symbols F and A have a different meaning than for $\boldsymbol{q}_1$. Let us apply the projection operator formula (A.1) for searching the basis functions of the representation Γ_1.

$$\begin{aligned} PS_{1x} &= (1\cdot\tilde{1}+\omega\cdot\tilde{c}_y)S_{1x} = S_{1x}+\omega\cdot\tilde{c}_yS_{1x} = S_{1x}+\omega(-S_{2x}\mathrm{e}^{-2\pi iq_z}) \\ &= S_{1x}-S_{2x}\mathrm{e}^{-3\pi iq_z} = S_{1x}-bS_{2x} = A_x \quad (\text{with } b=\mathrm{e}^{-3\pi iq_z}) \qquad \text{(A.2)} \\ PS_{1y} &= (1\cdot\tilde{1}+\omega\cdot\tilde{c}_y)S_{1y} = S_{1y}+\omega\cdot\tilde{c}_yS_{1y} = S_{1y}+\omega(S_{2y}\,\mathrm{e}^{-2\pi iq_z}) \\ &= S_{1y}+S_{2y}\mathrm{e}^{-3\pi iq_z} = S_{1y}+bS_{2y} = F_y \qquad \text{(A.3)} \\ PS_{1z} &= (1\cdot\tilde{1}+\omega\cdot\tilde{c}_y)S_{1z} = S_{1z}+\omega\cdot\tilde{c}_yS_{1z} = S_{1z}+\omega(-S_{2z}\mathrm{e}^{-2\pi iq_z}) \\ &= S_{1z}-S_{2z}\mathrm{e}^{-3\pi iq_z} = S_{1z}-bS_{2z} = A_z. \qquad \text{(A.4)} \end{aligned}$$

The same procedure allows obtaining the basis functions of the representation Γ_2. Then, for instance, the Fourier components corresponding to the representation Γ_1 are

$$\boldsymbol{S}_1(\boldsymbol{q}_2) = (u, v, w); \qquad \boldsymbol{S}_2(\boldsymbol{q}_2) = (-u, v, -w)\mathrm{e}^{-3\pi iq_z}.$$

If $q_z = 1/3$ then the phase factor is $\mathrm{e}^{-3\pi iq_z} = -1$ and we have for the representation Γ_1:

$$\boldsymbol{S}_1(\boldsymbol{q}_2) = (u, v, w); \qquad \boldsymbol{S}_2(\boldsymbol{q}_2) = (u, -v, w).$$

These real Fourier coefficients, together with the arm $\boldsymbol{q}_2^2$, define a sinusoidal modulated magnetic structure.

References

[1] Schobinger-Papamantellos P, Rodriguez-Carvajal J, Janssen T and Buschow K H J *Conf. Proc. 'Aperiodic 94' Les Diablerets*
[2] Hahn Th (ed) 2002 *International Tables for Crystallography* vol A (Dordrecht: Kluwer)
[3] Koptsik V A 1966 *Shubnikov Groups* (Moscow: Moscow University)
[4] Rodríguez-Carvajal J 1993 *Physica* B **192** 55 The programs of the `FullProf` *Suite* and their corresponding documentation can be obtained from the Web at http://www.ill.fr/dif/soft/fp/
[5] Chapon L C and Rodríguez-Carvajal J, unpublished
[6] Schobinger-Papamantellos P, de Mooij D B and Buschow K H J 1988 *J. Less-Common Met.* **144** 265
Schobinger-Papamantellos P, de Mooij D B and Buschow K H J 1988 *Z. Krist.* **185** 183
[7] Schobinger-Papamantellos P and Buschow K H J 1989 *J. Less-Common Met.* **146** 279
[8] Venturini G, Ijjaali I and Malaman B 1999 *J. Alloys Compounds* **288** 183
[9] Rossat-Mignod J 1987 *Methods of Experimental Physics: Neutron Scattering* vol 3 (New York: Academic)
[10] Bertaut E F 1963 *Magnetism III* ed G T Rado and H Suhl (New York: Academic) chapter 4 , p 149
[11] Izyumov Y A and Naish V E 1979 *J. Magn. Magn. Mater.* **12** 239
Izyumov Y A, Naish V E and Syromiatnikov V N 1979 *J. Magn. Magn. Mater.* **12** 249
Izyumov Y A, Naish V E and Petrov S B 1979 *J. Magn. Magn. Mater.* **13** 267
Izyumov Y A, Naish V E and Petrov S B 1979 *J. Magn. Magn. Mater.* **13** 275
Izyumov Y A 1980 *J. Magn. Magn. Mater.* **21** 33
[12] Brown P J 1986 Magnetic structure *Frontiers of Neutron Scattering* ed R J Birgeneau, D E Moncton and A Zeilinger (North-Holland: Elsevier Science) p 31
[13] Rodríguez-Carvajal J, Program `Moment` unpublished
[14] Schobinger-Papamantellos P, Janssen T and Buschow K H J 1996 *J. Magn. Magn. Mater.* **154** 29
[15] Schobinger-Papamantellos P, André G, Rodríguez-Carvajal J and Buschow K H J 1996 *J. Alloys Compounds* **232** 165
[16] Abert K, Meyer H J and Hoffmann R 1993 *J. Solid State Chem.* **106** 201
[17] Kimura I 1985 *J. Magn. Magn. Mater.* **52** 199
Kimura I 1988 *J. Magn. Magn. Mater.* **70** 273
[18] Kimura T, Iwata N, Ikeda T and Shigeoka T 1988 *J. Magn. Magn. Mater.* **76/77** 191
[19] Moriya T 1960 *Phys. Rev.* **120** 91
[20] Dzyaloshinskii I E 1957 *Sov. Phys.—JETP* **5** 1259
[21] Kimura I 1990 *J. Magn. Magn. Mater.* **86** 240